ETH Library

Electrically active defects induced by thermal oxidation and post-oxidation annealing of n-type 4H-SiC

Journal Article

Author(s):
Kumar, Piyush; Bathen, Marianne; Martins, Maria I.M.; Prokscha, Thomas; Grossner, Ulrike

Publication date:
2024-05-14

Permanent link:
https://doi.org/10.3929/ethz-b-000672253

Rights / license:
Creative Commons Attribution 4.0 International

Originally published in:
Journal of Applied Physics 135(18), https://doi.org/10.1063/5.0205965

Funding acknowledgement:
192218 - Understanding processing-induced defects to improve semiconductor device manufacturing technology (SNF)

This page was generated automatically upon download from the ETH Zurich Research Collection.
For more information, please consult the Terms of use.

Journal of Applied Physics | ARTICLE | pubs.aip.org/aip/jap

Electrically active defects induced by thermal oxidation and post-oxidation annealing of n-type 4H-SiC

Cite as: J. Appl. Phys. **135**, 185704 (2024); doi: 10.1063/5.0205965
Submitted: 28 February 2024 · Accepted: 25 April 2024 ·
Published Online: 9 May 2024

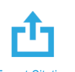

View Online Export Citation CrossMark

P. Kumar,[1,a)] M. E. Bathen,[1] M. I. M. Martins,[1,2] T. Prokscha,[2] and U. Grossner[1]

AFFILIATIONS

[1]Advanced Power Semiconductor Laboratory, ETH Zürich, Physikstrasse 3, 8092 Zurich, Switzerland
[2]Laboratory for Muon Spin Spectroscopy, Paul Scherrer Institute, Forschungsstrasse 111, 5232 Villigen, PSI, Switzerland

Note: This paper is part of the special topic, Defects in Semiconductors 2024.
[a)]**Author to whom correspondence should be addressed:** kumar@aps.ee.ethz.ch

ABSTRACT

In this work, we have performed a detailed study of the defects created in the bulk of 4H-SiC after thermal oxidation and post oxidation annealing using deep level transient spectroscopy and minority carrier transient spectroscopy (MCTS). The study reveals the formation of several shallow and deep level majority carrier traps in the bandgap. The ON1 ($E_C - 0.85$ eV), ON2a ($E_C - 1.05$ eV), and ON2b ($Ec - 1.17$ eV) levels are the most dominant and are observed across all the samples (E_C denotes the conduction band edge). Three shallow levels Ti(k) ($E_C - 0.17$ eV), $E_{0.23}$ ($E_C - 0.23$ eV), and $C_{1/2}$ ($E_C - 0.36/0.39$ eV) are observed in the samples. For most of the majority carrier defects, the highest concentration is observed after an NO anneal at 1300 °C. This behavior is sustained in the depth profile measurements where the defect concentration after the NO anneal at 1300 °C is significantly higher than for the rest of the samples. The origin of most of the majority carrier defects has been attributed to C interstitial injection from the interface during thermal oxidation and annealing. MCTS measurements reveal two prominent minority carrier traps, labeled $O_{0.17}$ ($E_V + 0.17$ eV) and B ($E_V + 0.28$ eV), where the concentration of $O_{0.17}$ is independent of annealing parameters while the concentration of the B level increases after the NO anneal (E_V denotes the valence band edge). Furthermore, the depth profiles of the defects are used to evaluate their diffusion parameters by solving the diffusion equation to fit the experimental profiles. The defect concentrations decay exponentially with depth, which evidences that the defects were created at or near the SiO_2–SiC interface and migrate toward the bulk during oxidation and post-oxidation annealing.

© 2024 Author(s). All article content, except where otherwise noted, is licensed under a Creative Commons Attribution (CC BY) license (https://creativecommons.org/licenses/by/4.0/). https://doi.org/10.1063/5.0205965

13 May 2024 10:15:02

I. INTRODUCTION

Thermal oxidation of 4H-SiC is one of the most crucial steps in the fabrication of power devices such as metal oxide semiconductors field effect transistors (MOSFETs). However, the interface created after thermal oxidation of 4H-SiC is known to contain a high density of interface traps (D_{it}), almost two orders of magnitude higher than its Si counterpart.[1,2] Present at or near the interface, these traps have the potential to negatively impact the transport of carriers and cause threshold voltage instabilities in the devices.[3] These traps further lead to significant reduction of carrier mobility and consequently lead to an increase in the channel resistance.[4] Annealing of the oxide–semiconductor device in a blacknitric oxide (NO) blackenvironment has been shown to improve the interface quality, reduce the D_{it} by almost an order of magnitude, and lead to a significant improvement in channel mobility [5] blackRecent studies have however shown that annealing in an NO environment can result in the generation of border traps[6] near the SiO_2–SiC interface,[7–9] which can lead to threshold voltage shifts and bias temperature instabilities[10] in the resulting device. blackThe impact of NO anneal is not limited to the interface and the near interface region and can extend to the bulk of SiC. Studies with low-energy muon spin rotation spectroscopy[11] and scanning capacitance microscopy[12] revealed that N introduced during NO anneal can lead to a counter doping in the near interface region extending up to ∼50 nm in SiC. Furthermore, deep level transient

© Author(s) 2024

TABLE I. Description of sample preparation and processing steps.

Sample name	Oxidation parameters	Oxide thickness (nm)	POA parameters
1300 ×	32 min at 1300 °C	48	…
1300NO1150	30 min at 1300 °C	48	70 min at 1150 °C in NO ambience
1300NO1300	28 min at 1300 °C	56	70 min at 1300 °C in NO ambience
1300Ar1300	32 min at 1300 °C	48	70 min at 1300 °C in Ar ambience

spectroscopy (DLTS) and minority carrier transient spectroscopy (MCTS) studies[13,14] revealed that annealing at high temperature can lead to the formation of several deep level defects in SiC which can lead to degradation of carrier lifetime by acting as recombination centers.[15]

Thermal oxidation for Si was well explained by the Deal–Groove model[16] and with modifications also explains the oxidation process and growth rate for SiO_2 on 4H-SiC.[17] The changes to the model included the oxidation of C and the out-diffusion of CO and CO_2 from the oxide– semiconductor interface to the surface of the sample. Furthermore, Hijikata *et al.*[18–20] proposed the emission of C and Si in their model to account for the reduced interface reaction rate. The C and Si emission during the thermal oxidation occurs into both the oxide and the SiC and is one of the methods to eliminate any existing carbon vacancies (V_C) in the material.[21] Although the emission of carbon interstitials (C_i) has the benefit of reducing the lifetime limiting $Z_{1/2}$ defect[15,22,23] in SiC, the injection of C is also responsible for the creation of new deep level defects in the SiC crystal. Okuda *et al.*[13] have demonstrated that defects are created in 4H-SiC after thermal oxidation and monitored their evolution after post oxidation annealing (POA) in Ar environment. Most of the defects were attributed to be related to carbon interstitials (C_i). For n-type samples, three majority carrier traps were found using DLTS, and two minority carrier traps using MCTS, in the temperature range of 200–700 K. C_i-related defects have also been studied using a carbon cap to inject the C_i into the SiC in the absence of oxygen,[24] creating multiple deep level defects that partially overlap with those formed by thermal oxidation[13] and were assigned to interstitial carbon in various forms.

In this work, we perform a study of the deep-level defects that are induced by oxidation and POA (in NO and Ar) in the bulk of 4H-SiC epitaxial layers using DLTS and MCTS. Several defect levels have been identified in the bandgap and their capture parameters have been thoroughly investigated using isothermal DLTS and MCTS measurements. Depth profile measurements performed with isothermal DLTS and MCTS have also helped perform a diffusion simulation to extract the generation rate and diffusivity of the C_i during the oxidation and POA.

II. METHOD

For the experiments, four low doped n-type 4H-SiC samples with 30μm thick epitaxial layers have been used. The doping density in the epi-layers was 2.6×10^{15} cm^{-3} as determined by capacitance–voltage (CV) measurements. The epi-layers were grown on highly doped SiC substrates ($\sim 8 \times 10^{18}$ cm^{-3}). The samples were cleaned in a Piranha solution followed by Tetramethylammonium hydroxide (TMAH) and then a short HF dip was performed to remove any native oxide. The cleaned samples then underwent a dry thermal oxidation at 1300 °C and three of the four samples also received a POA in either NO or Ar environment. The processing details are shown in Table I.

The thermal oxide was etched in buffered HF solution and semi-transparent Ni-contacts were deposited on the 4H-SiC surface to create Schottky contacts on the samples. The semi-transparent contact consists of an initial 20 nm thin Ni layer of 1500 μm diameter. This thin contact layer allows light to penetrate through and reach the semiconductor which is needed for the MCTS measurements. On top of the thin layer of Ni, a smaller contact of 600 μm diameter and 100 nm thickness is deposited for electrical contact. DLTS and MCTS measurements were then performed on the Schottky diodes to probe the 4H-SiC bulk defects induced by thermal oxidation and POA.

The DLTS/MCTS measurements were performed using the FT 1030 HERA-DLTS system, while the data evaluation was performed using the software provided by PhysTech GmbH. The CV measurements were carried out using the Boonton 7200 high-precision capacitance meter at 1 MHz. For isothermal measurement with varying filling pulse, the fast pulse generator from Keysight (33500 series) was employed which allows the smallest pulse width of 16.8 ns. All the measurements are carried out inside the closed Helium cryostat from Janis connected to the compressor from Sumitomo. Temperature controller from Lakeshore (336) was used to regulate the sample temperature during the measurements.

The Schottky samples were characterized using DLTS and MCTS in the temperature range of 20–600 K. For DLTS, a reverse bias of −5 V is applied and the sample is pulsed to 0 V with a pulse width (t_p) of 100 ms. A period width (T_w) of 500 ms was used. During the MCTS measurements, the sample is kept at a reverse bias of −5 V and an optical pulse of 100 ms is applied using an LED with a wavelength of 365 nm and a power of 200 mW. A Fourier transform of the recorded transients was performed using up to 28 correlation functions. The DLTS/MCTS signal shown in the rest of the paper refers to the coefficient of the sine term (b_1) in the Fourier series of the deep level or minority carrier transient Fourier spectroscopy (DLTFS/MCTFS).[25] Furthermore, iso-thermal measurements at the peak of each defect in the DLTS/MCTS spectrum were performed to measure the accurate capture cross section (σ_{meas}) and to extract the depth profile of the defects. For capture cross section measurements the t_p is varied from 20 to 500 ns at a fixed reverse bias (−5 V), temperature and T_W (500 ms). Furthermore, the depth profile was extracted by varying the reverse bias from 0 to −25 V while keeping a fixed t_p, T_W and temperature. The λ correction was taken into account during the calculation of the defect concentration.

13 May 2024 10:15:02

© Author(s) 2024

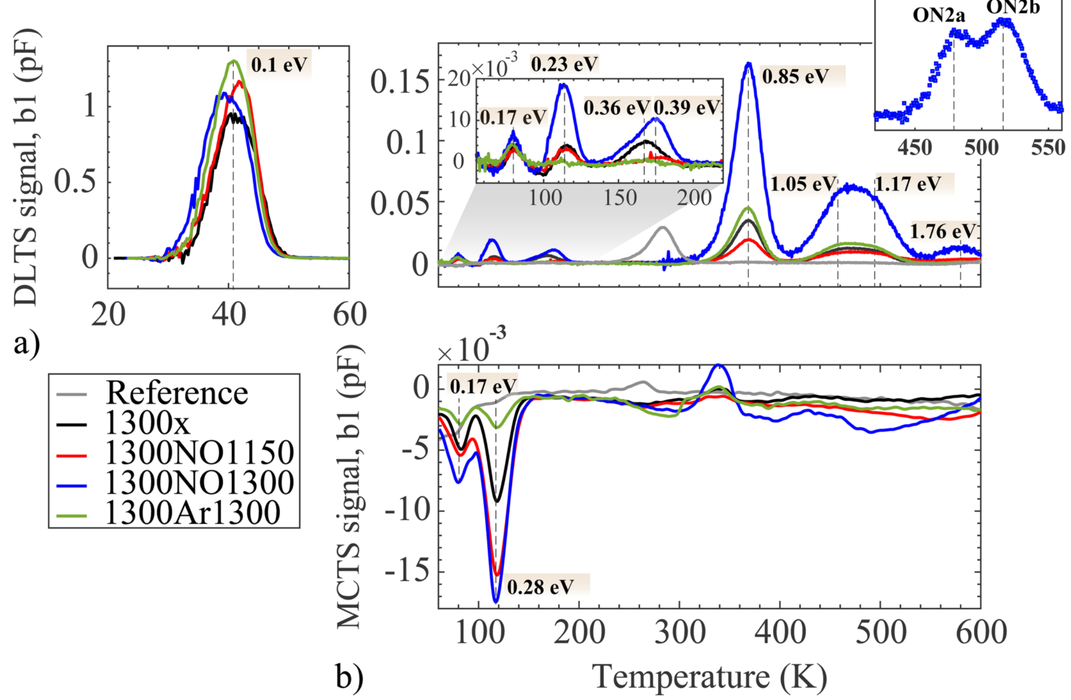

FIG. 1. (a) DLTS spectra of the thermally oxidized and annealed samples. Several defect levels are observed in the spectra after thermal oxidation in comparison to the reference sample. The defect concentration is affected by the POA condition and, remarkably, the peak heights and consequently the defect concentrations are substantially increased after annealing in NO environment at 1300 °C. (b) MCTS spectra of the thermally oxidized and annealed samples. Two dominant defects are observed in the low temperature region where the peak height is also affected by the annealing condition and the highest defect concentrations are observed after the NO anneal at 1300 °C.

13 May 2024 10:15:02

III. RESULTS AND DISCUSSION

A. Majority carrier traps

Figure 1(a) shows the recorded DLTS spectra for the four Schottky contact samples. Defect parameters for the majority carrier trap such as energy level, apparent, and measured capture cross section, and trap concentration across the four samples, are summarized in the top portion of Table II. Close to 40 K, the first peak is observed for all the samples and corresponds to an energy of (95–100) meV below the conduction band. Similar levels have

TABLE II. Summary of the defects and their parameters observed in the Schottky samples using DLTS/MCTS after thermal oxidation and post-oxidation annealing. The parameters include the defect label (Name), the energy level position (eV) below the conduction band edge (top table) or above the valence band edge (bottom table), apparent (σ_{app}), measured (σ_{meas}) capture cross section (cm^2), and the trap concentration (cm^{-3}) for each defect level and sample.

Name	Energy (eV)	σ_{app} (cm^2)	σ_{meas} (cm^2)	1300×	1300NO1150	1300NO1300	1300Ar1300
N(k)	0.095 ± 0.005	3.93×10^{-14}	…	3.31×10^{14}	3.36×10^{14}	3.46×10^{14}	4.04×10^{14}
Ti(k)	0.17	1.67×10^{-14}	4.62×10^{-15}	5.6×10^{11}	4.45×10^{11}	1.12×10^{12}	6.5×10^{11}
$E_0.23$	0.23	1.45×10^{-15}	1.89×10^{-15}	9.39×10^{11}	6.85×10^{11}	3.93×10^{12}	…
C_1	0.36	1.86×10^{-15}	2.78×10^{-15}	1.17×10^{12}	…	1.01×10^{12}	…
C_2	0.39	4.36×10^{-15}	1.19×10^{-15}	…	2.33×10^{11}	1.74×10^{12}	…
ON1	0.85	3.91×10^{-15}	8.23×10^{-16}	7.72×10^{12}	4.18×10^{12}	3.4×10^{13}	1.15×10^{13}
ON2a	1.05	2.51×10^{-15}	1.0×10^{-16}	2.69×10^{12}	1.51×10^{12}	1.26×10^{13}	3.37×10^{12}
ON2b	1.17	4.57×10^{-15}	1.06×10^{-15}	2.53×10^{12}	1.61×10^{12}	1.16×10^{13}	3.26×10^{12}
ON3	1.76	8.93×10^{-12}	…	…	6.84×10^{11}	2.47×10^{12}	…
$O_{0.17}$	0.17	1.0×10^{-14}	…	…	…	…	…
B	0.28	2.05×10^{-13}	…	1.40×10^{12}	3.28×10^{12}	3.65×10^{12}	7.59×10^{11}

© Author(s) 2024

been shown in the literature for the N-related centers in 4H-SiC.[26–29] Recently, Assmann *et al.*[30] studied the N-related center with high resolution DLTS and have shown the presence of N_C(k) at around 105 meV with triplet fine structures. As this level is present in all the measured samples, and the activation energy matches to the values shown in the literature, we assign this level to the N-related donor level at the substitutional cubic position.

The second peak is observed at ∼ 80 K and has an activation energy of 0.17 eV. Similar levels have been observed in the literature and correspond to a Ti related defect in the cubic position [Ti(k)].[31] Usually, a peak corresponding to a Ti defect at the hexagonal position is also observed in the literature, however, such a peak is absent in the measured spectra.

The third peak appears at around 120 K and corresponds to 230 meV below the conduction band edge E_C. As seen in Fig. 1 (a), the defect is present for the thermally oxidized and NO annealed samples but is absent in the Ar annealed samples. Additionally, the concentration of this defect is significantly increased after the 1300 °C NO anneal when compared to the pre-annealing case (1300×), while the 1150 °C NO anneal has little impact on the trap concentration of the 0.23 eV level. The defect is assigned a name $E_{0.23}$ and is expected to be created during thermal oxidation. Indeed, during NO annealing at 1300 °C, SiC also undergoes a continued thermal oxidation, which supports the formation of the defect $E_{0.23}$ during this process. Interestingly, we do not see any increase in the defect concentration for the NO annealed sample at 1150 °C, which indicates that the defect formation takes place at an elevated temperature closer to 1300 °C. For the Ar annealed sample, we observe a reduction in the concentration of this defect below the sensitivity of DLTS, indicating that annealing in Ar environment at 1300 °C can help eliminate this defect.

At around 165 K, corresponding to an energy level of 0.36 eV below the conduction band edge, another peak is observed for the non-annealed but oxidized sample (1300×). After 1300 °C NO annealing (1300NO1300), the feature clearly contains two contributions, at 0.36 and 0.39 eV below E_C. Both these peaks seem to be absent in the Ar-annealed sample. After the low-temperature (1150 °C) NO anneal, the 0.39 eV peak is only slightly visible and has one order of magnitude smaller concentration than for the 1300NO1300 sample. blackThe EH1 level is observed after electron irradiation[32] of 4H-SiC and has an activation energy of 0.45 eV while proton irradiation of 4H-SiC leads to the generation of M1 center at 0.42 eV below E_C.[33] Both EH1 and M1 center have activation energies, which is slightly higher but similar to the defect observed at ∼165 K in our spectrum. By performing isothermal annealing studies, Alfieri *et al.*[34] suggested that the EH centers are related to carbon interstitials (C_i). By comparing the M-center and the EH1 defects, KneŽević *et al.*[35] have shown that the two defects are indeed due to the C_is and arise from the same defect. Furthermore, Karsthof *et al.*[24] have performed C-injection using a C-cap and studied C_i related defects in 4H-SiC and observed a level, $E_{0.38}$, at 0.38 eV below E_C and have assigned it to be C_i related. This defect level has an activation energy, which is the closest to what is observed in our sample. Since, all the three defect species EH1, M1, and $E_{0.38}$ have properties similar to the observed defect at ∼165 K in our DLTS spectrum and as injection of C_i is also expected during thermal oxidation, the two defect levels at 0.36 and 0.39 eV below E_C are assumed to be related to the carbon interstitial. We have, therefore, named this defect as $C_{1/2}$ ($C_1 = 0.36$ eV, $C_2 = 0.39$ eV) for the rest of the paper. The absence of the C_1 defect in the 1150 °C NO annealed sample (1300NO1150) and of the $C_{1/2}$ defect from the 1300 °C Ar (1300Ar1300) annealed sample, could be a result of the migration of the C_i during the high temperature annealing process. In both these samples, no further oxidation occurs during the post oxidation annealing step and, therefore, no additional C_i is injected from the SiO_2–SiC interface into the SiC bulk. Therefore, the high temperature process only assists in the migration of the existing interstitials. For the 1300NO1300 sample, annealing in the NO environment at 1300 °C would also assist in the migration of the C_i. However, additional interstitials are also generated due to the continued thermal oxidation, which would preferentially be injected toward the SiC due to an already existing SiO_2 layer. Due to this, the concentration of the $C_{1/2}$ defect is increased after the NO annealing at 1300 °C when compared to the rest of the samples.

Compared to the reference sample, the $Z_{1/2}$ peak is not observed for either of the four oxidized samples and is expected to be annihilated upon injection of C_i during the oxidation process. The two dominant peaks after thermal oxidation, ON1 and ON2, are clearly observed in Fig. 1(a). These two peaks have been previously reported both after C-ion implantation,[36] thermal oxidation,[13,21] Al-implantation,[37] and C injection from carbon cap,[38] and are assumed to be associated with C_i. Compared to the non-annealed sample (1300×), the ON1 level ($E_C - 0.85$ eV) slightly increases after the Ar annealing. However, after an NO anneal at 1300 °C, the peak height and, consequently, the defect concentration significantly increases. A comparable trend is observed for the ON2 level where the peak height is substantially increased after the NO anneal at 1300 °C. One thing to note is that in both cases, the defect concentration is slightly reduced after the NO anneal at 1150 °C (compared to 1300×). Looking closely at the ON2 level, the peak appears to be broad and consists of two closely spaced but distinct contributions [see the inset of Fig. 1(a)]. The two contributions are named ON2a and ON2b and are associated with activation energies of $E_C - 1.05$ and -1.17 eV, respectively.

Finally, at a temperature of around 580 K, a peak labeled ON3 is visible in the DLTS spectrum at 1.76 eV below the conduction band edge [Fig. 1(a)]. This peak was also observed after thermal oxidation for 1.3 h at 1300 °C and after C^+ implantation in the work of Kawahara *et al.*[21] In our samples, this peak is only visible after thermal oxidation and subsequent annealing in NO at 1300 °C, indicating that an oxidation duration longer than 30 min is needed at 1300 °C for formation of ON3.

The apparent capture cross section (σ_{app}) of a defect level can be extracted from the extrapolation of the Arrhenius plot to $1/T = 0$. However, this method is prone to errors as a slight variation of the slope might lead to large variation in the intercept and consequently the calculated value. The second and more accurate method is to extract the measured capture cross section, σ_{meas}, by performing an isothermal DLTS measurement at the temperature corresponding to the peak maximum of the defect level under investigation. During this measurement, the filling pulse (t_p) is varied while keeping a fixed period width and temperature.[39] The

13 May 2024 10:15:02

© Author(s) 2024

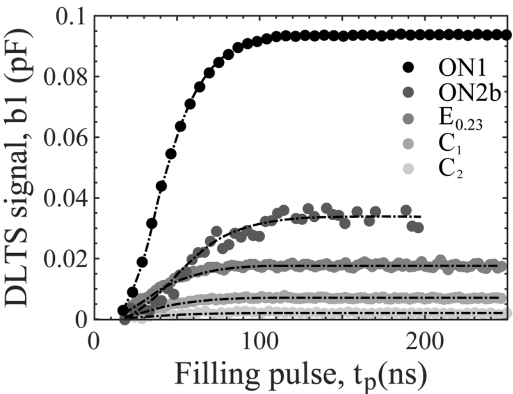

FIG. 2. Isothermal measurement performed with varying filling pulse to extract the measured capture cross section (σ_{meas}) of some of the defects for the sample annealed in NO environment at 1300 °C.

variation of the DLTS signal for five of the defects observed in the 1300NO1300 sample as a function of varying t_p is shown in Fig. 2. The capture cross sections extracted using both the above methods are summarized in Table II, where σ_{app} is calculated from the Arrhenius plot while σ_{meas} is the value extracted from the isothermal DLTS measurements.

To investigate the stability of the defect levels, a second round of measurements were performed on the samples. A comparison of the DLTS spectra for the 1300NO1300 sample before and after reverse bias annealing to 600 K (during the first DLTS run) is shown in Fig. 3. Although the data in the second round of measurements are noisy after 470 K, the ON1 and ON2 levels are clearly visible and do not appear to change in concentration. The ON3 level could not be observed in the second measurement round. In the lower end of the spectrum, the Ti(k) and $E_{0.23}$ defects also seem to be stable between different measurement rounds. The C_1 level, on the other hand, is reduced in concentration after exposure to 600 K, and the C_2 level appears to be slightly diminished as well. The same trend was observed for the C_1 peak in the 1300× sample (not shown).

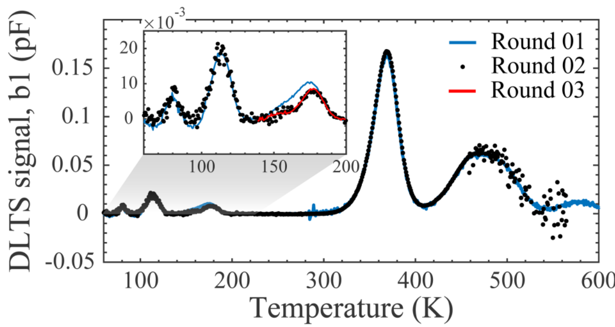

FIG. 3. Comparison of the DLTS spectrum recorded for the 1300NO1300 sample in two complete consecutive rounds and a third measurement around the $C_{1/2}$ level. The spectrum is replicated for all the defects except the C_1 and C_2 in the second round of measurement. In the third round of the measurement, no further variation in the $C_{1/2}$ was observed.

As mentioned above, the appearance of the $C_{1/2}$ level at around 170 K and 0.36–0.39 eV below E_C corresponds closely to the EH1,[32] M_1,[33] and $E_{0.38}$[24] levels. The M-center is known to appear in two configurations, where in configuration A, M_1 ($E_C - 0.42$ eV) appears in a pair with M_3 ($E_C - 0.74$ eV), while in configuration B, M_2 (Ec − 0.65 eV) and M_4 ($E_C - 0.86$ eV) appear in a pair.[35] Furthermore, due to a small activation barrier,[40] the two configurations can be interchanged by annealing and by applying a reverse bias voltage. While the $C_{1/2}$ level has energetic proximity to the M_1 level, no signature of its pair M_3 level is observed in our DLTS spectrum across all the samples. Interestingly, the ON1 level observed in our samples has a very similar activation energy to the M4 level. However, similar to the previous case, its pair the M2 level is also absent across our samples. Furthermore, the authors in Ref. 35 have shown that the M_1 and EH1 level arise from the same defect. By Laplace DLTS the authors also highlighted that the EH1 (or M1) level has a single emission line, whereas in this $C_{1/2}$ defect comprises of two defect levels.

Comparing the two rounds of measurements, all defects apart from the C_1 level are thermally stable up to an annealing temperature of (at least) 600 K. The absence of M_3 peak (pair of M_1) in the first measurement round, the M_2 peak in the second round of the measurement and no significant reduction in the concentration of C_2, and only slight reduction in the concentration of the C_1 level, indicate that the $C_{1/2}$ level has a different origin than the M_1 level. Similar considerations were made in Ref. 24 for the $E_{0.38}$ level. Interestingly, the using the high resolution weighting function, two components were revealed in the $E_{0.38}$ level, similar to what is observed in the $C_{1/2}$ level. A third round of measurement was performed around the $C_{1/2}$ level as shown in Fig. 3. No further variation in the concentration of the defect pair was observed.

13 May 2024 10:15:02

B. Minority carrier traps

The samples were also characterized with MCTS to observe the minority carrier traps created during high temperature oxidation and annealing. The results are shown in Fig. 1(b). The first dominant peak observed in the spectra is the $O_{0.17}$ ($E_V + 0.17$ eV), where E_V denotes the valence band edge. The $O_{0.17}$ corresponds closely to the X-peak observed in Ref. 41 after heavy ion irradiation and in Ref. 42 in as-grown 4H-SiC epi-layers. Several samples were investigated in Ref. 42 and the Al impurity on the Si site is assigned as the likely candidate for the origin of this defect. The next minority carrier trap is observed close to 120 K and assigned as the B peak and with an activation energy of 0.28 eV. *Ab initio* calculations have shown that boron can occupy the Si (B_{Si}) or C (B_C) sites and have activation energies of ~0.3 and 0.65 eV, respectively, above E_V.[43] MCTS measurements on Fe doped n-type 4H-SiC samples show two dominant minority carrier traps: shallow B and the D-center, with activation energies of $E_V + 0.27$ and +0.62 eV.[44] The shallow B level has been assigned to substitutional boron on the Si site[45] whereas the deeper-lying D-center is known to be B

© Author(s) 2024

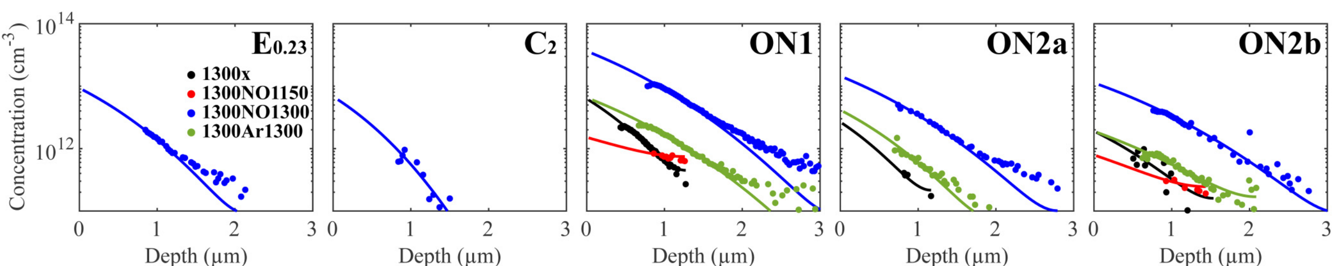

FIG. 4. Concentration profiles of the majority carrier traps extracted for the four samples under investigation. The dots are the experimental data while the fit is simulated by solving the diffusion equation.

related, although its exact origin is still being discussed. The main models being proposed for the D-center are B on the Si site next to a C vacancy,[46] and B on the C site.[47] Capan *et al.*[47] performed MCTS measurements on neutron irradiated n-type 4H-SiC and observed peaks at 0.27 eV and 0.6 eV above the valence band edge and associated these defects with B on Si (B_{Si}) and C (B_C) sites, respectively. Therefore, we would like to associate the defect level B observed in our samples with substitutional boron on the Si site. However, the increase in the defect concentration upon annealing in NO environment and the reduction in concentration upon annealing in Ar environment [see Fig. 1(b)] indicates that this defect level exists in the form of a complex, whose population is either enhanced or suppressed depending on the annealing environment. Alternatively, diffusion is taking place, leading to reduction or accumulation of the defect level within the probed region depending on the annealing conditions.

Similar behavior is observed for the $O_{0.17}$ ($E_V + 0.17$ eV) level, where the concentration changes with the annealing environment.

C. Defect diffusion

To investigate the variation of defect concentration from the near-surface toward the bulk of the semiconductor, we have performed iso-thermal DLTS and MCTS measurements, keeping a fixed pulse and period width while varying the reverse bias. Most of the majority carrier trapping defects in the DLTS spectra are associated with C-interstitials, which are assumed to be generated at/near the SiO_2–SiC interface during the oxidation process and migrate toward the bulk under high temperature. Therefore, to capture the dynamics of the generation and migration of the defects, we have performed a simulation to solve the diffusion equation [Eq. (1)] and extract the diffusivity and generation rate of the defects at the oxide–semiconductor interface

$$\frac{\partial[C_i]}{\partial t} = D_{ci}\frac{\partial^2[C_i]}{\partial x^2} + G_{ci}. \quad (1)$$

Here, $[C_i]$ is the concentration of the interstitial related defects, G_{ci} is the thermal generation rate, and D_{ci} is the diffusion coefficient of the defect. Furthermore, the diffusion coefficient of the defect can be modeled as

$$D_{ci} = D^0_{ci}\exp\left(\frac{-E_{mci}}{kT}\right). \quad (2)$$

Here, D^0_{ci} is a constant and assumed to be in the range of $10^{-3} - 10^{-2}\,cm^2/s$[48] and E_{mci} is the migration barrier.

The concentration profiles of the defects extracted from the iso-thermal measurements are shown in Fig. 4 (majority carrier traps) and Fig. 5 (minority carrier traps). The dots in the figures are the experimental data while the solid lines are the fits achieved after solving the diffusion equation. Equations (1) and (2) are solved for each of the measured defect profiles and the extracted parameters for the 1300NO1300 sample are summarized in Table III. The results from the simulation fit very well with the measured defect distributions and upon extrapolation provide a good estimate for the respective defect concentrations at the oxide–semiconductor interface. The measurements also show that the impact of the thermal oxidation is not limited only to the interface but can extend up to several micrometers into the semiconductor.

Depth profiles for the $E_{0.23}$ and C_2 levels could be extracted only for the 1300NO1300 sample, whereas the ON1, ON2a and ON2b levels could be studied for all thermally oxidized and annealed samples. The $E_{0.23}$ and C_2 defects showcase a low diffusivity (D_{ci}) and low generation rate (G_{ci}) when compared to the ON1/ON2 defects (see Table III). Due to this, the defects

13 May 2024 10:15:02

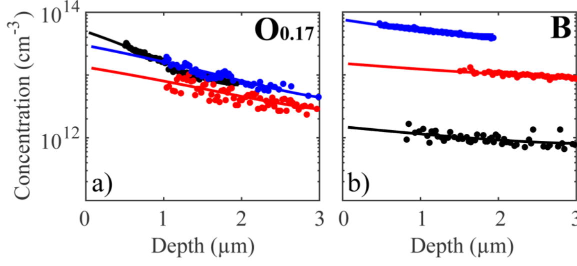

FIG. 5. Concentration profiles of the minority carrier traps extracted for the four samples under investigation. The dots are the experimental data while the fit is simulated by solving the diffusion equation.

© Author(s) 2024

TABLE III. Diffusion parameters of the defects in sample 1300NO1300; diffusivity D_{ci} ($cm^{-2}s$), migration barrier E_{mci} (eV), and thermal generation rate G_{mci} ($cm^{-3}s$). The energy barriers are given as a range following the assumed value of the exponential pre-factor for diffusion, D^0_{ci}, at 0.001–0.01 $cm^2\ s^{-1}$.

Defect	D_{ci} (cm^2s^{-1}) (10^{-12})	E_{mci} (eV)	G_{ci} ($cm^{-3}s$) (10^{10})
$E_{0.23}$	1.22	2.78–3.10	3.83
C_2	0.78	2.84–3.16	1.25
ON1	1.99	2.72–3.03	12.7
ON2a	1.92	2.72–3.03	5.71
ON2b	2.52	2.69–3.00	4.53
$O_{0.17}$	8.74	2.52–2.83	20.1
B	29.8	2.35–2.66	1.75

responsible for the $E_{0.23}$ and C_2 levels do not diffuse deep into the sample, and beyond a depth of 2 μm, they have concentrations lower than the sensitivity limit of the equipment. In contrast, the ON1 defect has slightly higher D_{ci} and significantly higher G_{ci}. At the same time the diffusion barrier for the ON1 defect is also slightly reduced in comparison to the $E_{0.23}$ and C_2 defects. Due to these three reasons, it can be observed that the ON1 defect has a much higher concentration and diffuses as deep as 3 μm into the 1300NO1300 sample (see Fig. 4). In the case of the 1300Ar1300 sample, no further generation of defects is expected during Ar annealing at 1300 °C as there is no continued oxidation. However, the defects generated during thermal oxidation can migrate under the influence of high temperature. Thus, the ON1 defect is present at a depth of up to 3 μm for the 1300Ar1300 sample as well, although the defect concentration is reduced significantly when compared to the 1300NO1300 sample. Similar behavior is observed for the ON2a and ON2b defects where the defect profile for the 1300Ar1300 sample has similar shape as for the 1300NO1300 sample but is reduced in concentration. In the case of 1300×, the defects do not have enough time to diffuse into the sample due to lack of annealing and, therefore, the concentration of defects falls below the sensitivity limit of the equipment beyond ~1 μm.

The minority carrier depth profile has been extracted for the thermally oxidized (1300×) and NO annealed (1300NO1150, 1300NO1300) samples. Depth profiles of the minority carrier defects could not be extracted for the Ar annealed (1300Ar1300) sample. In Fig. 5, it can be observed that both the traps $O_{0.17}$ and B exhibit relatively flat depth profiles when compared to the majority carrier traps. Assuming that these traps are also generated during thermal oxidation and diffuse either during oxidation or annealing, the calculated value of D_{ci} is very high when compared to the majority carrier traps, indicating a swift diffusion of defects in the sample. Another plausible and more likely scenario is that these defect species are introduced into the sample during epitaxial growth (see also Ref. 42), and are, therefore, uniformly distributed throughout the sample resulting in a flat depth profile. Interestingly, the depth profile of the $O_{0.17}$ defect level appears to be similar for the three samples with defect concentration. In contrast, the depth profile of the B peak for the three samples [Fig. 5(b)] has three very distinct behavior where the defect concentration for the 1300NO1300 sample is significantly higher in comparison to the 1300NO150 sample, which in turn is almost an order of magnitude higher in concentration than the 1300× sample.

Overall, the concentration vs depth profiles for the majority carrier traps (Fig. 4) exhibit a reduction toward the sample bulk, confirming an injection mechanism from the near-surface region. The diffusion range varies depending on the oxidation and annealing conditions.

IV. CONCLUDING REMARKS

In this work, we have performed a study of the majority and minority carrier defects generated in the bulk of SiC as a result of thermal oxidation and post oxidation annealing. It is observed that while thermal oxidation of SiC at 1300 °C results in an elimination of the carbon vacancies ($Z_{1/2}$), it leads to a simultaneous generation of several shallow ($E_{0.23}$, C1/2), and deep level (ON1 and ON2) majority carrier defects. POA in NO environment at 1300 °C leads to a significant increase in the concentration of each defect, whereas the anneal in Ar environment at 1300 °C results in the reduction of the $E_{0.23}$ and C1/2 defects. We conclude that most of the defects are related to C-interstitials (C_i) injected during thermal oxidation from the SiO_2–SiC interface. Continued thermal oxidation and consequent injection of C_i during NO anneal at 1300 °C is responsible for the increase in the defect concentrations. Anneal in Ar environment leads to the migration of existing C-species in the SiC bulk without additional oxidation, resulting in the reduction of the shallow majority carrier defects. Isothermal measurements of these defects were performed to extract an accurate capture cross section (σ_{meas}) and their depth profiles. Diffusion of defect species was observed up to a depth of 3 μm after NO/Ar anneal at 1300 °C. Additionally, by solving the diffusion equation on the extracted depth profile of the defects, generation and diffusion parameters of the defects have been calculated.

Furthermore, two minority carrier defects were also observed, namely, the $O_{0.17}$ and the B center. The $O_{0.17}$ defect is likely due to the Al (on the Si site) introduced into the epitaxial layer during growth. The flat and overlapping depth profile of this defect across all the samples support the hypothesis. The B center observed in our sample is associated with boron on the Si site, where boron, like Al, is expected to be introduced during the epitaxial growth. However, contrary to the $O_{0.17}$, the B defect has a dependence on the annealing environment and temperature. While anneal in Ar environment leads to a substantial reduction in the concentration of the B center, NO anneal at both low (1150 °C) and high temperature (1300 °C) leads to an increase in the concentration of the B center.

13 May 2024 10:15:02

ACKNOWLEDGMENTS

This work is supported by the Swiss National Science Foundation under Grant No. 192218. The work of M.E.B. was supported by an ETH Zürich Postdoctoral Fellowship.

AUTHOR DECLARATIONS

Conflict of Interest

The authors have no conflicts to disclose.

© Author(s) 2024

Author Contributions

P. Kumar: Conceptualization (equal); Data curation (equal); Formal analysis (equal); Investigation (equal); Methodology (equal); Validation (equal); Visualization (equal); Writing – original draft (equal); Writing – review & editing (equal). **M. E. Bathen:** Conceptualization (equal); Investigation (equal); Methodology (equal); Writing – review & editing (equal). **M. I. M. Martins:** Conceptualization (equal); Writing – review & editing (equal). **T. Prokscha:** Conceptualization (equal); Funding acquisition (equal); Supervision (equal); Writing – review & editing (equal). **U. Grossner:** Conceptualization (equal); Funding acquisition (equal); Project administration (equal); Resources (equal); Supervision (equal); Writing – review & editing (equal).

REFERENCES

[1] N. S. Saks, S. S. Mani, and A. K. Agarwal, Appl. Phys. Lett. **76**, 2250 (2000).
[2] C. Langpoklakpam, A.-C. Liu, K.-H. Chu, L.-H. Hsu, W.-C. Lee, S.-C. Chen, C.-W. Sun, M.-H. Shih, K.-Y. Lee, and H.-C. Kuo, Crystals **12**, 245 (2022).
[3] S. Yu, M. Kang, T. Liu, D. Xing, A. Salemi, M. H. White, and A. K. Agarwal, in *2019 IEEE 7th Workshop on Wide Bandgap Power Devices and Applications (WiPDA)* (IEEE, 2019), pp. 420–424.
[4] J. Müting and U. Grossner, Mater. Sci. Forum. **924**, 693 (2018).
[5] S. Dhar, S. Wang, J. R. Williams, S. T. Pantelides, and L. C. Feldman, MRS Bull. **30**, 288 (2005).
[6] D. Fleetwood, Microelectron. Reliab. **80**, 266 (2018).
[7] P. Kumar, M. Krummenacher, H. G. Medeiros, S. Race, P. Natzke, I. Kovacevic-Badstubner, and U. Grossner, "Exploring the border traps near the SiO2-SiC interface using conductance measurements," *International Reliability Physics Symposium* (2024).
[8] H. Yoshioka, T. Nakamura, and T. Kimoto, J. Appl. Phys. **115**, 014502 (2014).
[9] J. R. Nicholls, A. M. Vidarsson, D. Haasmann, E. O. Sveinbjörnsson, and S. Dimitrijev, J. Appl. Phys. **129**, 054501 (2021).
[10] T. Grasser, Microelectron. Reliab. **52**, 39 (2012).
[11] P. Kumar, M. I. M. Martins, M. E. Bathen, J. Woerle, T. Prokscha, and U. Grossner, Phys. Rev. Appl. **19**, 054025 (2023).
[12] P. Fiorenza, F. Giannazzo, M. Vivona, A. La Magna, and F. Roccaforte, Appl. Phys. Lett. **103**, 153508 (2013).
[13] T. Okuda, G. Alfieri, T. Kimoto, and J. Suda, Appl. Phys. Express. **8**, 111301 (2015).
[14] L. Knoll, L. Kranz, and G. Alfieri, Mater. Sci. Forum. **963**, 309 (2019).
[15] K. Danno, D. Nakamura, and T. Kimoto, Appl. Phys. Lett. **90**, 202109 (2007).
[16] B. E. Deal and A. S. Grove, J. Appl. Phys. **36**, 3770 (1965).
[17] Y. Song, S. Dhar, L. C. Feldman, G. Chung, and J. R. Williams, J. Appl. Phys. **95**, 4953 (2004).
[18] Y. Hijikata, H. Yaguchi, and S. Yoshida, Appl. Phys. Express. **2**, 021203 (2009).
[19] Y. Hijikata, S. Yagi, H. Yaguchi, and S. Yoshi, in *Physics and Technology of Silicon Carbide Devices*, edited by Y. Hijikata (InTech, 2012).
[20] Y. Hijikata, Diamond. Relat. Mater. **92**, 253 (2019).
[21] K. Kawahara, J. Suda, and T. Kimoto, J. Appl. Phys. **111**, 053710 (2012).
[22] K. Danno and T. Kimoto, J. Appl. Phys. **100**, 113728 (2006).
[23] H. M. Ayedh, R. Nipoti, A. Hallén, and B. G. Svensson, J. Appl. Phys. **122**, 025701 (2017).
[24] R. Karsthof, M. Etzelmüller Bathen, A. Kuznetsov, and L. Vines, J. Appl. Phys. **131**, 035702 (2022).
[25] S. Weiss and R. Kassing, Solid-State Electron. **31**, 1733 (1988).
[26] W. Götz, A. Schüner, G. Pensl, W. Suttrop, W. J. Choyke, R. Stein, and S. Leibenzeder, J. Appl. Phys. **73**, 3332 (1993).
[27] T. Kimoto, A. Itoh, H. Matsunami, S. Sridhara, L. L. Clemen, R. P. Devaty, W. J. Choyke, T. Dalibor, C. Peppermüller, and G. Pensl, Appl. Phys. Lett. **67**, 2833 (1995).
[28] J. Pernot, W. Zawadzki, S. Contreras, J. L. Robert, E. Neyret, and L. Di Cioccio, J. Appl. Phys. **90**, 1869 (2001).
[29] S. Kagamihara, H. Matsuura, T. Hatakeyama, T. Watanabe, M. Kushibe, T. Shinohe, and K. Arai, J. Appl. Phys. **96**, 5601 (2004).
[30] N. Assmann, C. Persson, A. Y. Kuznetsov, and E. V. Monakhov, Appl. Phys. Lett. **119**, 262101 (2021).
[31] T. Dalibor, G. Pensl, H. Matsunami, T. Kimoto, W. J. Choyke, A. Schöner, and N. Nordell, Phys. Status Solidi A **162**, 199 (1997).
[32] C. Hemmingsson, N. T. Son, O. Kordina, J. P. Bergman, E. Janzén, J. L. Lindström, S. Savage, and N. Nordell, J. Appl. Phys. **81**, 6155 (1997).
[33] H. Nielsen, D. Martin, P. Lévêque, A. Hallén, and B. Svensson, Phys. B **340–342**, 743 (2003).
[34] G. Alfieri and A. Mihaila, J. Phys.: Condens. Matter. **32**, 465703 (2020).
[35] T. Knežević, A. Hadžipašić, T. Ohshima, T. Makino, and I. Capan, Appl. Phys. Lett. **120**, 252101 (2022).
[36] L. Storasta, J. P. Bergman, E. Janzén, A. Henry, and J. Lu, J. Appl. Phys. **96**, 4909 (2004).
[37] P. Kumar, M. Martins, M. Bathen, T. Prokscha, and U. Grossner, Mater. Sci. Semicond. Process. **174**, 108241 (2024).
[38] M. E. Bathen, R. Karsthof, A. Galeckas, P. Kumar, A. Yu, U. Grossner, and L. Vines, Mater. Sci. Semicond. Process **176**, 108316 (2024).
[39] A. Khan and Y. Masafumi, in *Solar Cells—New Approaches and Reviews*, edited by L. A. Kosyachenko (InTech, 2015).
[40] J. Coutinho, J. D. Gouveia, T. Makino, T. Ohshima, Z. Pastuovic, L. Bakrac, T. Brodar, and I. Capan, Phys. Rev. B **103**, L180102 (2021).
[41] N. Für, M. Belanche, C. Martinella, P. Kumar, M. E. Bathen, and U. Grossner, IEEE Trans. Nucl. Sci. **70**(8), 1892–1899 (2023).
[42] M. E. Bathen, P. Kumar, M. Ghezellou, M. Belanche, L. Vines, and U. Grossner, Mater. Sci. Semicond. Process **177** (2024).
[43] V. J. B. Torres, I. Capan, and J. Coutinho, Phys. Rev. B **106**, 224112 (2022).
[44] F. C. Beyer, C. G. Hemmingsson, S. Leone, Y.-C. Lin, A. Gällström, A. Henry, and E. Janzén, J. Appl. Phys. **110**, 123701 (2011).
[45] J. Zhang, L. Storasta, J. P. Bergman, N. T. Son, and E. Janzén, J. Appl. Phys. **93**, 4708 (2003).
[46] P. G. Baranov, I. V. Il'in, and E. N. Mokhov, Phys. Solid State **40**, 31 (1998).
[47] I. Capan, T. Brodar, Y. Yamazaki, Y. Oki, T. Ohshima, Y. Chiba, Y. Hijikata, L. Snoj, and V. Radulović, Nucl. Instrum. Methods Phys. Res., Sec. B **478**, 224 (2020).
[48] J. Philibert, *Atom Movements: Diffusion and Mass Transport in Solids* (éditions de Physique Les Ulis, 1991).

13 May 2024 10:15:02

© Author(s) 2024